

# Concurrent Task Scheduling and Dynamic Voltage and Frequency Scaling in a Real-Time Embedded System with Energy Harvesting

Xue Lin, *Student Member, IEEE*, Yanzhi Wang, *Student Member, IEEE*, Naehyuck Chang, *Fellow, IEEE*, and Massoud Pedram, *Fellow, IEEE*

**Abstract**—Energy harvesting is a promising technique to overcome the limit on energy availability and increase the lifespan of battery-powered embedded systems. In this paper, the question of how one can achieve the prolonged lifespan<sup>1</sup> of a real-time embedded system with energy harvesting capability (RTES-EH) is investigated. The RTES-EH comprises a photovoltaic (PV) panel for energy harvesting, a supercapacitor for energy storage, and a real-time sensor node as the embedded load device. A global controller performs simultaneous optimal operating point tracking for the PV panel, state-of-charge (SoC) management for the supercapacitor, and energy-harvesting-aware real-time task scheduling with dynamic voltage and frequency scaling (DVFS) for the sensor node, while employing a precise solar irradiance prediction method. The controller employs a cascaded feedback control structure, where an outer supervisory control loop performs real-time task scheduling with DVFS in the sensor node while maintaining the optimal supercapacitor SoC for improved system availability, and an inner control loop tracks the optimal operating point of the PV panel on the fly. Experimental results show that the proposed global controller lowers the task instance drop rate by up to 63% compared with the baseline controller within the same service time (i.e., from sunrise to sunset.)

**Index Terms**—Energy harvesting, real-time embedded system, photovoltaic panel, supercapacitor.

## I. INTRODUCTION

ENERGY consumption is one of the most important design criteria for battery-powered devices and systems. Dynamic power management (DPM) [2][3][4][5] and dynamic

voltage and frequency scaling (DVFS) [6][7][8][9] techniques have been extensively investigated for reducing energy consumption of battery-powered systems while meeting performance targets. However, even with sophisticated DPM or DVFS techniques, batteries still need to be charged or replaced for sustained system operation.

There are some applications that do not allow battery charging or replacement, such as sensor nodes deployed in radioactive surroundings. Therefore, *energy harvesting* techniques have been deployed to overcome the limit of energy source and increase the lifespan of untethered embedded systems [10][11][12]. Energy harvesting from ambient energy sources including sunlight, wind, and tidal wave can provide unlimited and inexhaustible power supply for embedded systems. However, the harvested energy exhibits intermittency characteristics. For instance, the output power of a photovoltaic (PV) panel at noon is an order of magnitude higher than that in the morning or evening. Therefore, an energy storage element, typically a rechargeable battery [10] or a supercapacitor [12], is mandatory in an embedded system with energy harvesting capability for sustainable power supply. Several prototypes have been presented such as Heliomote [10] and Prometheus [11]. An interesting summary of various design considerations for an embedded system with energy harvesting is provided in [13].

A number of recent work have focused on power minimization algorithms and techniques for a *real-time embedded system with energy harvesting capability* (RTES-EH) [14][15][16]. These work are different from the traditional real-time task scheduling and DVFS work [6][7][8][9] because of the intermittent nature of harvested energy and limited size of the energy storage element. Indeed, the primary purpose of the RTES-EH task scheduling is to enhance the *system availability* in spite of the sporadic nature of the harvested energy. The lazy scheduling algorithm proposed in [14] executes tasks as late as possible but at full speed. DVFS combined with lazy scheduling is used [15][16] to reduce deadline miss rate minimizing energy dissipation.

In this work, we present a *global control algorithm* for a RTES-EH comprised of a PV panel as the energy harvesting source, a supercapacitor as the energy storage element, and a real-time sensor node as the embedded load device. The presented global controller performs simultaneous optimal

A preliminary version of this paper was presented at *IEEE International Symposium on Low Power Electronics and Design (ISLPED)*, Beijing, China, Aug. 2013 [1].

X. Lin and M. Pedram are with University of Southern California, Los Angeles, CA 90089, USA (e-mail: xuelin@usc.edu, pedram@usc.edu).

Y. Wang is with Syracuse University, Syracuse, NY, 13210, USA (e-mail: ywang393@syr.edu).

N. Chang is with Korea Advanced Institute of Science and Technology, Daejeon, 305-701, Korea (e-mail: naehyuck@cad4x.kaist.ac.kr).

<sup>1</sup> The lifetime of a battery is usually less than five years, and in this work we propose to use supercapacitor instead of battery for embedded systems to prolong the lifespan of the whole system to more than 20 years.

operating point tracking of the PV panel, state-of-charge (SoC) management of the supercapacitor, as well as real-time task scheduling with DVFS for the sensor node. The combined task scheduler and DVFS manager in turn relies on a precise solar irradiance prediction method.

Limitations of the previous work and key contributions of the present work are summarized in the following.

- 1) Using battery as the energy storage element in previous work [14][15][16] may prevent a RTES-EH from having a long lifespan. Typically, batteries have a rather short cycle life (up to several hundred charge-discharge cycles) after which they have to be replaced. Alternatively, supercapacitors constitute a highly effective energy storage element for a RTES-EH due to (i) orders-of-magnitude longer cycle life than batteries, (ii) higher power capacity to deal with bursty power demands of load devices, and (iii) very low environmental impact [17]. Because the terminal voltage variation of a supercapacitor is much larger than that of a battery [18], it is not possible to apply previous work directly to the supercapacitor-based RTES-EH. In this work, we present a global control algorithm for a supercapacitor-based RTES-EH, accounting for supercapacitor characteristics.
- 2) The converters connecting the energy source to the energy storage element, and the energy storage element to the load device cause power loss in a RTES-EH. The power loss is significant in a supercapacitor-based RTES-EH due to large variation of the supercapacitor terminal voltage. The present work considers the converter efficiency variation based on accurate power converter modeling in order to optimize the overall system availability (this is in clear contrast to previous work which assumes 100% power conversion efficiency).
- 3) Most of the previous work assumes ideal component models for both the energy harvesting source and the energy storage element. The present work employs accurate component models to take into account the nonlinear current-voltage (I-V) characteristics of the PV panel, and energy loss and self-discharge of the supercapacitor when optimizing the system availability.
- 4) To derive a global control algorithm for the RTES-EH with a PV panel as the energy harvesting source, it is necessary to predict the solar irradiance profile, and thereby, estimate the PV panel energy generation profile. The present work uses an accurate solar irradiance prediction algorithm, which refines the solar irradiance prediction at each decision epoch based on actual solar irradiance values observed previously.

To develop an effective global control algorithm, there are two fundamental subproblems to be solved, i.e., the *supercapacitor charging* problem and the *converter-aware frequency setting* problem. The first problem aims at dynamically maximizing the supercapacitor charging current by optimally setting the operating point of the PV panel (this is similar to the problem discussed in [18][19]). Different from the traditional *maximum power point tracking* (MPPT) techniques [20], which only focus on maximizing the output

power of the PV panel itself, the supercapacitor charging problem accounts for the power loss in the converter to maximize the input power to the supercapacitor. The second problem focuses on finding the optimal sensor node execution frequency for a single task instance without deadline constraint such that the amount of energy extracted from the supercapacitor is minimized. According to [21], the minimum execution frequency in the sensor node is no longer always optimal in energy saving for a task instance without deadline constraint when the converter power loss is taken into account.

Based on the optimal solutions to the aforesaid two subproblems and the PV panel energy generation profile, we present a near-optimal global control algorithm by using a cascaded feedback control structure. An outer supervisory control loop maintains the supercapacitor SoC throughout the system operational period (from sunrise to sunset) so as to enhance the overall system availability and reduce the task instance drop rate. The supercapacitor SoC maintenance is achieved through effective real-time task scheduling combined with DVFS as well as selective task instance dropping in the sensor node. An inner control loop, on the other hand, tracks the optimal operating point of the PV panel (and hence the input current of the supercapacitor) on the fly to maximize the amount of harvested energy. Experimental results demonstrate that the proposed accurate component model-based global control algorithm on the RTES-EH significantly lowers the task instance drop rate by up to 63% compared with baseline control algorithm.

The remainder of this paper is organized as follows. Section II presents models of components in the RTES-EH. Section III introduces the RTES-EH architecture and the real-time task set. Section IV defines a formal problem formulation of the RTES-EH global control problem. And Section V provides the optimal solutions to the aforesaid subproblems. Section VI discusses about the solar irradiance prediction algorithm. Section VII proceeds with the global control algorithm. Section VIII and IX are experimental results and conclusion, respectively.

## II. COMPONENT MODELS

### A. PV Cell Model and Characterization

As stated before, the energy harvesting source in the RTES-EH is a PV panel. The PV panel consists of a number of PV cells connected together in a balanced series/parallel configuration i.e., an  $m \times n$  array, where  $m$  is the number of PV cells connected in series and  $n$  is the number of PV cells connected in parallel. We use  $V_{pv}$  and  $I_{pv}$  to denote the output voltage and current of the PV panel, respectively, and  $V_{pv,c}$  and  $I_{pv,c}$  to denote the output voltage and current of a single PV cell inside the panel, respectively. The output voltages and currents have the following relationships:

$$V_{pv} = m \cdot V_{pv,c}, \quad I_{pv} = n \cdot I_{pv,c}. \quad (1)$$

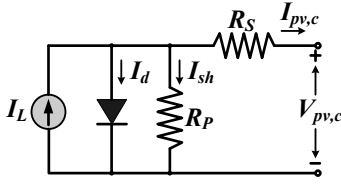


Fig. 1. An equivalent circuit model of a PV cell.

A typical equivalent circuit model of a PV cell is shown in Fig. 1, with I-V characteristics given by:

$$I_{pv,c} = I_L - I_d - I_{sh} \quad (2)$$

$$= I_L(G) - I_0(T) \left( e^{\frac{(V_{pv,c} + I_{pv,c} R_s) \cdot q}{A k T}} - 1 \right) - \frac{V_{pv,c} + I_{pv,c} R_s}{R_p},$$

where

$$I_L(G) = \frac{G}{G_{STC}} \cdot I_L(G_{STC}), \quad (3)$$

and

$$I_0(T) = I_0(T_{STC}) \cdot \left( \frac{T}{T_{STC}} \right)^3 \cdot e^{\frac{q E_g}{A k} \cdot \left( \frac{1}{T_{STC}} - \frac{1}{T} \right)}. \quad (4)$$

Parameters in (2) – (4) are defined as follows.  $G$  denotes the solar irradiance level;  $T$  is the cell temperature;  $q$  is the charge of the electron;  $E_g$  is the energy bandgap; and  $k$  is the Boltzmann's constant. STC stands for *standard test condition* in which the irradiance level is 1000 W/m<sup>2</sup> and the cell temperature is 25 °C. There are still five unknown parameters, which are typically not provided by manufacturers, yet to be determined. These unknown parameters are:

- $I_L(G_{STC})$ : photo-generated current at STC,
- $I_0(T_{STC})$ : dark saturation current at STC,
- $R_s$ : PV cell series resistance,
- $R_p$ : PV cell parallel (shunt) resistance, and
- $A$ : ideality factor of the diode.

We adopt the method proposed in [22] to extract the above-mentioned five unknown parameters from the measured PV cell I-V curve at any specific environmental condition.

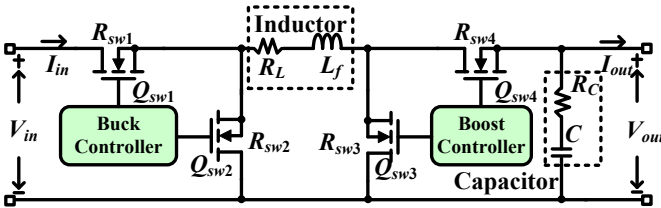


Fig. 2. PWM buck-boost power converter architecture.

### B. Power Converter Model

Both the charger and the DC-DC converter used in the RTES-EH are programmable PWM (pulse width modulation) buck-boost power converters. A charger regulates its output current to the value set by the micro-controller, while a DC-DC converter regulates its output voltage to the value set

by the micro-controller. Fig. 2 shows a conceptual structure of the PWM buck-boost power converter. We denote the input voltage, input current, output voltage, and output current of the power converter by  $V_{in}$ ,  $I_{in}$ ,  $V_{out}$ , and  $I_{out}$ , respectively. The power loss of the converter,  $P_{conv}$ , consists of the conduction loss, the switching loss and the controller loss [23].

According to the energy conservation law,  $P_{conv}$  satisfies:

$$V_{in} \cdot I_{in} = P_{conv} + V_{out} \cdot I_{out}. \quad (5)$$

Based on the relationship between  $V_{in}$  and  $V_{out}$ , the power converter operates in one of the two possible operating modes: the buck mode when  $V_{in} > V_{out}$  and the boost mode, otherwise. When the converter is operating in the buck mode, its power loss  $P_{conv}$  is given by

$$P_{conv} = I_{out}^2 \cdot (R_L + H \cdot R_{sw1} + (1 - H) \cdot R_{sw2} + R_{sw4}) \quad (6)$$

$$+ \frac{(\Delta I)^2}{12} \cdot (R_L + H \cdot R_{sw1} + (1 - H) \cdot R_{sw2} + R_{sw4} + R_C)$$

$$+ V_{in} \cdot f_s \cdot (Q_{sw1} + Q_{sw2}) + V_{in} \cdot I_{controller},$$

where  $H = V_{out}/V_{in}$  is the PWM duty ratio and  $\Delta I = V_{out} \cdot (1 - H)/(L_f \cdot f_s)$  is the maximum current ripple;  $f_s$  is the switching frequency;  $I_{controller}$  is the current flowing into the micro-controller of the power converter;  $R_L$  and  $R_C$  are the internal series resistances of the inductor  $L$  and the capacitor  $C$ , respectively;  $R_{swi}$  and  $Q_{swi}$  are the turn-on resistance and gate charge of the  $i$ -th MOSFET switch shown in Fig. 2, respectively.

On the other hand, the converter power loss  $P_{conv}$  in the boost mode is given by

$$P_{conv} = \left( \frac{I_{out}}{1 - H} \right)^2 \cdot (R_L + H \cdot R_{sw3} + (1 - H)R_{sw4} + R_{sw1} + H(1 - H)R_C) \quad (7)$$

$$+ \frac{(\Delta I)^2}{12} (R_L + H R_{sw3} + (1 - H)(R_{sw4} + R_C) + R_{sw1})$$

$$+ V_{out} \cdot f_s \cdot (Q_{sw3} + Q_{sw4}) + V_{in} \cdot I_{controller},$$

where  $H = 1 - V_{in}/V_{out}$  and  $\Delta I = V_{in} \cdot H/(L_f \cdot f_s)$ .

It can be observed from (6) and (7) that the converter power loss  $P_{conv}$  is a function of  $V_{in}$ ,  $V_{out}$ , and  $I_{out}$ . Notice that  $P_{conv}$  can also be written as a function of  $V_{in}$ ,  $I_{in}$ ,  $V_{out}$ , which is not provided in this paper due to space limitation.

### C. Supercapacitor Model

Supercapacitors have a very small internal resistance and thus very small IR power loss is incurred during charging and discharging. Supercapacitors also exhibit a significantly higher volumetric power density and a longer cycle life compared with batteries [17]. These features make supercapacitors a good choice for energy storage element in a RTES-EH.

A primary disadvantage of supercapacitors is the full-range terminal voltage variation as a function of its SoC. The terminal voltage of a supercapacitor, denoted by  $V_{cap}$ , is a linear function of its SoC denoted by  $Q_{cap}$ . More precisely,

$V_{cap} = Q_{cap}/C_{cap} = \sqrt{2E_{cap}/C_{cap}}$ , where  $E_{cap}$  is the energy stored in the supercapacitor and  $C_{cap}$  is the capacitance of the supercapacitor. The terminal voltage variation of a supercapacitor leads to power conversion efficiency variation in the RTES-EH, which motivates us to address this issue in the proposed global control algorithm.

Moreover, a supercapacitor may lose as much as 40% of its energy per day due to self-discharge [17]. The terminal voltage decay of a supercapacitor after a time period  $\Delta t$  is given by:

$$V_{cap}(t + \Delta t) = V_{cap}(t) \cdot e^{-\frac{\Delta t}{\Gamma}}, \quad (8)$$

when no external power supply or load is connected to the supercapacitor. The parameter  $\Gamma$  in (8) denotes the *self-discharge time constant*.

### III. REAL-TIME EMBEDDED SYSTEM WITH ENERGY HARVESTING CAPABILITY

#### A. System Architecture

This paper investigates a RTES-EH with the architecture shown in Fig. 3. In particular, the RTES-EH is comprised of a PV panel as the energy harvesting source, a supercapacitor as the energy storage element, a real-time DVFS-enabled sensor node as the load device, and power converters connected in between. A charger connects the PV panel to the supercapacitor, and a DC-DC converter connects the supercapacitor to the real-time sensor node. A micro-controller controls the system operation and executes the control algorithm of the system.

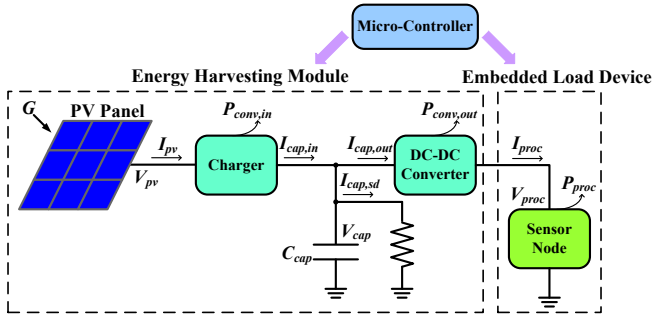


Fig. 3. Block diagram of the RTES-EH.

The RTES-EH operates from sunrise  $T_{sunrise}$  until sunset  $T_{sunset}$  (i.e., the system operational period) and it is in idle state for the rest of time during a day. We denote the solar irradiance and temperature on the PV panel at time  $t$  by  $G(t)$  and  $T(t)$ , respectively. Since the temperature has only secondary effect on the I-V characteristics of the PV panel, we do not consider the PV panel temperature change in this paper, i.e., we assume constant PV panel temperature  $T(t) = T_{STC}$ . On the other hand,  $G(t)$  has a huge impact on the I-V characteristics of the PV panel. We thus estimate the  $G(t)$  profile by using a novel and highly accurate solar irradiance prediction method as shall be discussed in Section VI. We

denote the output voltage and current of the PV panel at time  $t$  by  $V_{pv}(t)$  and  $I_{pv}(t)$ , respectively. We control the PV panel operating point  $(V_{pv}(t), I_{pv}(t))$  through effectively setting the charger output current  $I_{cap,in}(t)$  as shown in Fig. 3.

We denote the terminal voltage, input current and output current of the supercapacitor at time  $t$  by  $V_{cap}(t)$ ,  $I_{cap,in}(t)$ , and  $I_{cap,out}(t)$ , respectively. The supercapacitor energy  $E_{cap}(t)$  at time  $t$  is given by

$$E_{cap}(t) = E_{cap}(T_{sunrise}) + \int_{T_{sunrise}}^t V_{cap}(\tau) (I_{cap,in}(\tau) - I_{cap,out}(\tau) - I_{cap,sd}(\tau)) d\tau, \quad (9)$$

where  $E_{cap}(T_{sunrise})$  is the initial supercapacitor energy at time  $T_{sunrise}$ , and  $I_{cap,sd}(t)$  is the self-discharge current at time  $t$ , which is calculated based on (8).

We assume a single-core microprocessor as the sensor node in the RTES-EH. We denote the supply voltage, the input current, and the power consumption of the sensor node by  $V_{proc}(t)$ ,  $I_{proc}(t)$  and  $P_{proc}(t)$ , respectively. The sensor node has  $N$  discrete operating frequencies:  $freq_{min} = freq_1 < freq_2 < \dots < freq_N = freq_{max}$ ; each operating frequency  $freq_n$  corresponds to a supply voltage  $V_{proc,n}$ , an input current  $I_{proc,n}$ , and a power consumption value  $P_{proc,n}$  ( $1 \leq n \leq N$ ).

The input voltage, input current, output voltage, and output current of the charger are  $V_{pv}(t)$ ,  $I_{pv}(t)$ ,  $V_{cap}(t)$ , and  $I_{cap,in}(t)$ , respectively. The charger power loss at time  $t$ , denoted by  $P_{conv,in}(t)$ , is a function of  $V_{pv}(t)$ ,  $I_{pv}(t)$ , and  $V_{cap}(t)$  as discussed in Section II.B. Similarly, the power loss of the DC-DC converter, denoted by  $P_{conv,out}(t)$ , is a function of its input voltage, output voltage, and output current, i.e.,  $V_{cap}(t)$ ,  $V_{proc}(t)$ , and  $I_{proc}(t)$ , respectively. The following two equations hold due to the energy conservation law:

$$V_{pv}(t)I_{pv}(t) = V_{cap}(t)I_{cap,in}(t) + P_{conv,in}(t), \quad (10)$$

$$V_{cap}(t)I_{cap,out}(t) = V_{proc}(t)I_{proc}(t) + P_{conv,out}(t). \quad (11)$$

#### B. Real-Time Task Set

In this paper, we assume a frame-based, preemptive, hard real-time task set in the sensor node [8]. The set of  $M$  real-time periodic tasks is denoted by  $\{\mathcal{T}_1, \mathcal{T}_2, \dots, \mathcal{T}_M\}$ . Task instances of  $\mathcal{T}_i$  ( $1 \leq i \leq M$ ) are released periodically with a period of  $D_i$ , which is also the relative deadline of task instances of  $\mathcal{T}_i$ . Task instances of  $\mathcal{T}_i$  have a workload of  $W_i$ , which is given as the number of clock cycles required to complete a task instance. We use the independent-task assumption that tasks (and therefore task instances) are independent from each other [13][14][15].

We define the frame length as  $T_{LCM}$ , which is the *hyper-period* of all the tasks (i.e., the least common multiple of  $D_1, D_2, \dots, D_M$ ). We use  $K = \frac{T_{sunset} - T_{sunrise}}{T_{LCM}}$  to denote the total number of frames from  $T_{sunrise}$  to  $T_{sunset}$ . Therefore, each  $k$ -th frame ( $1 \leq k \leq K$ ) begins at time  $T_{sunrise} + (k -$



1)  $\cdot T_{LCM}$  and ends at time  $T_{sunrise} + k \cdot T_{LCM}$ . Fig. 4 shows the start time and end time of the  $k$ -th frame and also the time windows of task instances in the frame. The duration of a frame is in the order of minutes or seconds, which is much shorter than the RTES-EH operational period. We use 5 minutes for  $T_{LCM}$  in the simulation to represent a reasonable trade-off between computational complexity and control accuracy of the global control algorithm.

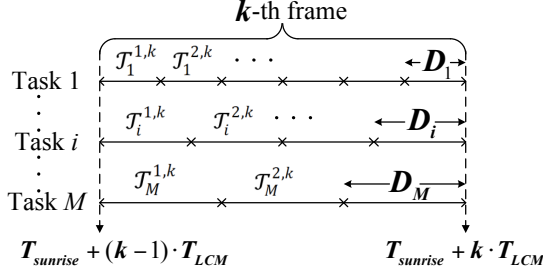


Fig. 4. Task instances in the  $k$ -th frame.

The *earliest deadline first* (EDF) scheduling [6] is incorporated in the sensor node to schedule the periodic tasks. The  $j$ -th ( $1 \leq j \leq T_{LCM}/D_i$ ) task instance of  $\mathcal{T}_i$  in the  $k$ -th frame, denoted by  $\mathcal{T}_i^{j,k}$ , is released at time  $T_{sunrise} + (k-1)T_{LCM} + (j-1)D_i$ , which is the absolute release time of that task instance. Hence, the absolute deadline of task instance  $\mathcal{T}_i^{j,k}$  is equal to  $T_{sunrise} + (k-1)T_{LCM} + jD_i$ .

#### IV. PROBLEM FORMULATION

We use  $fs_i(t)$  to denote the sensor node operating frequency assigned for executing an instance of  $\mathcal{T}_i$  at time  $t$ . For real implementation, we assume that  $fs_i(t)$  can only take discrete values in the set  $\{freq_1, freq_2, \dots, freq_N\}$ . If the sensor node does not execute any task instances of  $\mathcal{T}_i$  at time  $t$ , we have  $fs_i(t) = 0$ . The single-core microprocessor assumption of the sensor node ensures that at most one of the  $fs_i(t)$  values for  $1 \leq i \leq M$  at time  $t$  is non-zero. Therefore the operating frequency of the sensor node  $fs(t) = \sum_{1 \leq i \leq M} fs_i(t)$ . We adopt a general definition of a *schedule* of task instances where task instance dropping or timing constraint violation is allowed to accommodate the intermittent nature of the harvested energy of the RTES-EH [15][16]. We define a new variable  $\mathcal{S}_i^{j,k}$  such that  $\mathcal{S}_i^{j,k} = 1$  indicates the completion of task instance  $\mathcal{T}_i^{j,k}$  before its deadline, i.e.,

$$\int_{T_{sunrise} + (k-1)T_{LCM} + (j-1)D_i}^{T_{sunrise} + (k-1)T_{LCM} + jD_i} fs_i(t) dt \geq W_i. \quad (12)$$

On the other hand,  $\mathcal{S}_i^{j,k} = 0$  indicates the task instance  $\mathcal{T}_i^{j,k}$  has missed the deadline, i.e.,

$$\int_{T_{sunrise} + (k-1)T_{LCM} + (j-1)D_i}^{T_{sunrise} + (k-1)T_{LCM} + jD_i} fs_i(t) dt < W_i. \quad (13)$$

We minimize the task instance drop rate, or equivalently, we maximize total number of fully executed task instances, given by

$$Total\_Executed = \sum_{1 \leq k \leq K} \sum_{1 \leq i \leq M} \sum_{1 \leq j \leq T_{LCM}/D_i} \mathcal{S}_i^{j,k}. \quad (14)$$

The power consumption  $P_{proc}(t)$  and supply voltage  $V_{proc}(t)$  of the sensor node are dependent on  $fs(t)$ . The supercapacitor discharging current  $I_{cap,out}(t)$  is determined by  $P_{proc}(t)$ ,  $P_{conv,out}(t)$ , and  $V_{cap}(t)$ , using (11). The supercapacitor charging current  $I_{cap,in}(t)$  is determined by  $(V_{pv}(t), I_{pv}(t))$ ,  $P_{conv,in}(t)$ , and  $V_{cap}(t)$ , using (10). We calculate  $E_{cap}(t)$ , i.e., the energy stored in the supercapacitor at time  $t$ , using (9). Therefore, the  $fs_i(t)$  profiles for  $1 \leq i \leq M$  and the PV panel operating point  $(V_{pv}(t), I_{pv}(t))$  are the control variables of the RTES-EH. We achieve the supercapacitor SoC control (i.e., the control of its energy) through task scheduling with DVFS (i.e., finding the  $fs_i(t)$  profiles) and PV panel operating point tracking.

The formal statement of the global control problem for the RTES-EH is given as follows:

#### RTES-EH global control problem statement:

**Given** the initial supercapacitor energy  $E_{cap}(T_{sunrise})$ ,

**Find** a schedule and frequency allocation of all tasks, represented by  $fs_i(t)$  ( $1 \leq i \leq M$ ), and the PV panel operating point  $(V_{pv}(t), I_{pv}(t))$  for  $t \in [T_{sunrise}, T_{sunset}]$ ,

**Maximize** the total number of fully executed task instances by the deadline, as given by (14),

**Subject to** the energy conservation law (9), (10), and (11).

Please note that the solar irradiance profile  $G(t)$  is not given explicitly in the problem statement. Instead,  $G(t)$  will be estimated by a prediction method in the global control algorithm. In the next three sections, we will introduce two optimization subproblems and their solutions, the solar irradiance prediction algorithm, and the global control algorithm based on the solutions to the subproblems and solar irradiance prediction.

#### V. OPTIMIZATION SUBPROBLEMS

We first define two fundamental optimization subproblems that are necessary in solving the original global control problem. The two subproblems are the *supercapacitor charging* (SC) problem and the *converter-aware frequency setting* (CA-FS) problem. These two subproblems are inherent from the architecture of the RTES-EH as shown in Fig. 3. According to the energy flow in the RTES-EH, the RTES-EH can be partitioned into two parts, i.e., the energy harvesting part and the energy consumption part. The energy harvesting part consists of the PV panel, the supercapacitor and the charger in between. The energy consumption part consists of the supercapacitor, the sensor node and the converter in between. For the energy harvesting part, one natural question is how to collect the maximum amount of energy from the PV

panel to the supercapacitor, and the SC problem answers the question. For the energy consumption part, one natural question is what is the optimal sensor node frequency such that the energy extracted from the supercapacitor is minimized, and the CA-FS problem answers the question.

#### A. Supercapacitor Charging (SC) Problem

The SC problem aims at maximizing the supercapacitor charging current  $I_{cap,in}(t)$  by optimally setting the operating point  $(V_{pv}(t), I_{pv}(t))$  of the PV panel, given the current solar irradiance  $G(t)$  and the amount of energy stored in supercapacitor  $E_{cap}(t)$ . Solving the SC problem optimally at any time  $t \in [T_{sunrise}, T_{sunset}]$  is required for the optimal solution to the global control problem for the RTES-EH. The SC problem is nontrivial and requires close examination of characteristics of both the PV panel and the charger.

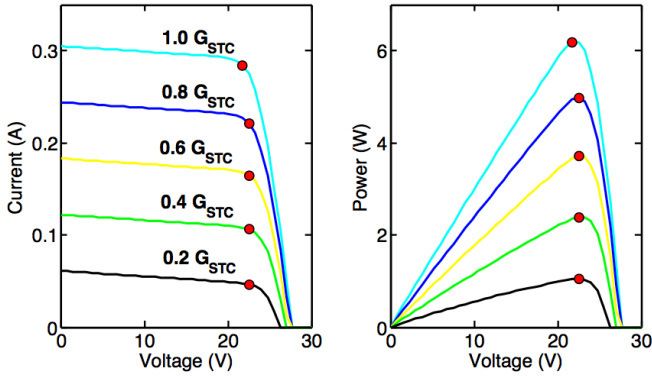


Fig. 5. I-V and P-V characteristics of the PV panel under different solar irradiance values.

Fig. 5 illustrates the I-V and power-voltage (P-V) characteristics of the PV panel under different solar irradiance  $G$  values. For a specific  $G$  value, the PV panel output current  $I_{pv}$  decreases as the output voltage  $V_{pv}$  increases, and the PV panel output power  $V_{pv} \cdot I_{pv}$  is maximized when it operates at the *maximum power point* (MPP), marked by red dots in Fig. 5. Conventional *MPP tracking* (MPPT) technique maintains the PV panel operating point at its MPP. However, such technique cannot guarantee the maximum amount of energy transferred into the supercapacitor due to the neglect of efficiency variation of the charger [18]. Recent *maximum power transfer tracking* (MPTT) technique takes into account the non-ideal behavior of the charger, thereby maximizing the energy transferred into the supercapacitor [18]. In this paper, we adopt the MPTT technique to solve the SC problem optimally at any time  $t \in [T_{sunrise}, T_{sunset}]$ .

There are two possible implementations of the SC problem solution. The first one is software-based or model-based implementation whereas the second one is hardware-based implementation. The former implementation uses accurate PV panel modeling as described in Section II.A and derives the optimal supercapacitor charging current  $I_{cap,in}(t)$ . This implementation is adopted in the supervisory control of the RTES-EH. On the other hand, the latter implementation is

based on a perturb and observe (P&O) heuristic in a hardware micro-controller to dynamically track the optimal operating point of the PV panel. This implementation is adopted in the inner control loop of the RTES-EH and does not need prior knowledge of the PV panel modeling.

#### B. Converter-Aware Frequency Setting (CA-FS) Problem

The CA-FS problem aims at finding the optimal sensor node frequency for executing a specific task instance such that the energy extracted from the supercapacitor is minimized. Recall that executing a task instance at minimum clock frequency is not necessarily the minimum energy solution [21], because the power conversion efficiency of the DC-DC converter in the system is a function of the terminal voltage of the supercapacitor, which in turn is dependent on the amount of energy stored in the supercapacitor  $E_{cap}(t)$ .

We derive the total energy extracted from the supercapacitor during the execution of a task instance as a function of the execution frequency  $f$ . Note that  $f$  can only take discrete values from the set  $\{freq_1, freq_2, \dots, freq_N\}$ . The supply voltage and power consumption of the sensor node during execution of a task instance are functions of  $f$ , i.e.,  $V_{proc}(f)$  and  $P_{proc}(f)$ , respectively. The total execution time of a task instance of  $T_i$ , denoted by  $T_i^{exe}(f)$ , is given as  $T_i^{exe}(f) = W_i/f$ , where  $W_i$  is the workload of task instances of  $T_i$  as discussed in Section III.B. We assume that the  $V_{cap}$  value will not change significantly during the execution of a single task instance, since the execution time is too short to make noticeable SoC change in the supercapacitor. The power loss of the DC-DC converter during execution of a task instance is a function of its input voltage  $V_{cap}$ , output voltage  $V_{proc}(f)$ , and output current  $I_{proc}(f) = P_{proc}(f)/V_{proc}(f)$ , as specified in Section II.B. Therefore, we derive the power loss of the DC-DC converter as a function of  $f$  and  $V_{cap}$ , i.e.,  $P_{conv,out}(f, V_{cap})$ . The amount of energy extracted from the supercapacitor for executing a task instance of  $T_i$ , denoted by  $E_i^{extract}(f, V_{cap})$  is given as

$$E_i^{extract}(f, V_{cap}) = T_i^{exe}(f) \cdot (P_{proc}(f) + P_{conv,out}(f, V_{cap})), \quad (15)$$

which is not a monotonically increasing function of  $f$ . This implies that using the minimum clock frequency for task execution does not always minimize the total energy drawn from the supercapacitor. We denote the optimal sensor node frequency for executing a task instance of  $T_i$  by  $f_i^{opt}(V_{cap})$  that minimizes the total energy drawn from the supercapacitor.  $f_i^{opt}(V_{cap})$  is calculated as

$$f_i^{opt}(V_{cap}) = \operatorname{argmin}_{freq_{min} \leq f \leq freq_{max}} E_i^{extract}(f, V_{cap}). \quad (16)$$

## VI. SOLAR IRRADIANCE PREDICTION ALGORITHM

The solution to the global control problem relies on the

solar irradiance prediction results. In this section, we introduce a solar irradiance prediction algorithm based on [24]. From the start time  $T_{sunrise}$  to the end time  $T_{sunset}$  of the RTES-EH operational period, there are a total number of  $K$  frames of task instances to be executed, as mentioned in Section III.B. We assume that the solar irradiance is constant during a frame. This assumption is valid since the duration of a frame is in the order of minutes or seconds. Therefore, we will predict the solar irradiance for rest of the day at the start time of the  $k$ -th (for  $1 \leq k \leq K$ ) frame in the  $d$ -th day, i.e.,  $T_{s,k}^d$ , where subscript  $s$  denotes “start”.

For the solar irradiance prediction, an important observation is that the actual solar irradiance over the  $k$ -th frame in the  $d$ -th day may be viewed as the solar irradiance over the  $k$ -th frame in a sunny day multiplied by a *decay factor*, representing the effect of clouds, if the  $d$ -th day is cloudy. Obviously, the sunny day solar irradiance over the  $k$ -th frame varies with season changes. This effect is however captured by a *smoothing operation* as shall be discussed later. In general, the solar irradiance prediction algorithm consists of the initial prediction and the intra-day refinement: the initial prediction is performed at the beginning of each day i.e.,  $T_{s,1}^d$  to predict the sunny day solar irradiance over each frame during that day; the intra-day refinement is performed at the start time of the  $k$ -th (for  $1 < k \leq K$ ) frame in that day to predict the decay factors and thereby refining the prediction results over the rest of the frames in that day. Please note that at the start time of the  $k$ -th frame, the decay factor in the  $(k-1)$ -st frame is already known. And decay factors of different frames in the same day are positively correlated.

In the initial prediction phase, we adopt a variant of the well-known exponential average-based prediction method, in order for effectively predicting the sunny day solar irradiance in each frame of a day (please see the discussion below for the differences between our version and the standard method.) Consider that we are at time  $T_{s,1}^d = T_{sunrise}$  of the  $d$ -th day. We want to derive the prediction value of the sunny day solar irradiance in the  $k$ -th (for  $1 \leq k \leq K$ ) frame of that day, denoted by  $Predict_k^d$ , based on the prediction value of the sunny day solar irradiance in the  $k$ -th frame of the  $(d-1)$ -st day, denoted by  $Predict_k^{d-1}$ , and the actual solar irradiance in the  $k$ -th frame of the  $(d-1)$ -st day, denoted by  $G_k^{d-1}$ . Please note that we must also capture and predict the seasonal change of the sunny day solar irradiance, while filtering out random solar irradiance decay effects due to the presence of clouds. This is a smoothing operation. The  $Predict_k^d$  value is calculated as follows

$$Predict_k^d = \beta(Predict_k^{d-1}, G_k^{d-1}) \cdot G_k^{d-1} + (1 - \beta(Predict_k^{d-1}, G_k^{d-1})) \cdot Predict_k^{d-1}. \quad (17)$$

In the above equation, the learning rate function  $\beta(Predict_k^{d-1}, G_k^{d-1})$  is set to

$$\beta(Predict_k^{d-1}, G_k^{d-1}) = \begin{cases} \beta_0, & \text{if } Predict_k^{d-1} < G_k^{d-1} \\ \beta_0 e^{-\lambda(Predict_k^{d-1} - G_k^{d-1})}, & \text{otherwise} \end{cases} \quad (18)$$

where  $\beta_0$  is the basis learning rate, and  $\lambda$  is the decaying parameter for the learning rate.

The motivation for this smoothing operation is as follows. Since (i) we want to predict the seasonal change of the sunny day solar irradiance while filtering out the effect of clouds, and (ii)  $G_k^{d-1} \ll Predict_k^{d-1}$  only if there are clouds, it is natural that our new predicted sunny day solar irradiance  $Predict_k^d$  should not be so much influenced by  $G_k^{d-1}$  (which is strongly affected by the clouds.) Therefore, we adopt the exponentially decaying learning rate (18), rather than the constant learning rate in the original exponential average-based prediction method.

The intra-day refinement phase is performed at the start time of each  $k$ -th (for  $1 < k \leq K$ ) frame in a day to predict the decay factors and thereby refining the prediction results over the rest of the frames in that day. The intra-day refinement is implemented as follows. Consider that we are currently at the start time of the  $k$ -th frame in the  $d$ -th day, i.e.,  $T_{s,k}^d$ , and we intend to refine the prediction results of the solar irradiance in the  $\hat{k}$ -th (for  $k \leq \hat{k} \leq K$ ) frame of that day. We denote the results of the intra-day refinement as  $Refine_k^d$  (for  $k \leq \hat{k} \leq K$ ). Since at time  $T_{s,k}^d$  the actual solar irradiance in the  $(k-1)$ -st frame is already known, we calculate  $Refine_k^d$  by

$$Refine_k^d \leftarrow (1 - \gamma) \cdot Predict_k^d + \gamma \cdot \frac{G_{k-1}^d}{Predict_{k-1}^d} \cdot Predict_k^d, \quad (19)$$

where the coefficient  $0 < \gamma < 1$ . We learn the optimal  $\gamma$  value by using the stochastic gradient descent method [25]. Typically, a  $\gamma$  value in the range of [0.5, 0.7] will yield the best prediction results.

The intuition for (19) is as follows: if the actual solar irradiance in the  $(k-1)$ -st frame is higher than the predicted solar irradiance in that frame, i.e.,  $G_{k-1}^d > Predict_{k-1}^d$ , it is highly likely that the actual solar irradiance in the  $\hat{k}$ -th ( $k \leq \hat{k} \leq K$ ) frame of the same day will also be higher than the predicted solar irradiance in that frame, and vice versa. Experimental results in Section VIII will demonstrate that the prediction error can be reduced to 42% of the initial prediction error by using intra-day refinement.

## VII. GLOBAL CONTROL ALGORITHM

We propose a cascaded feedback control based algorithm, comprised of an outer supervisory control loop and an inner control loop, to effectively solve the global control problem. The outer supervisor control loop is performed at each decision epoch (to be defined later) of the RTES-EH operational period, and it maintains the supercapacitor SoC

through effective task scheduling with DVFS, as well as selective task dropping. The inner control loop performs the optimal PV panel I-V operating point setting. The outer supervisory control loop and the inner control loop are performed every 300 seconds (which is equal to the frame length  $T_{LCM}$ ) and five milliseconds, respectively, in this paper.

The decision epochs are defined as the start time of each frame. We denote the  $k$ -th (for  $1 \leq k \leq K$ ) decision epoch by  $T_{s,k}$ , where subscript  $s$  stands for “start” and  $T_{s,k} = T_{sunrise} + (k-1)T_{LCM}$ . At each decision epoch  $T_{s,k}$ , the supervisory control algorithm finds a schedule and frequency allocation of the task instances in the  $k$ -th frame, represented by  $f_{s_i}(t)$  (for  $1 \leq i \leq M$  and  $t \in [T_{s,k}, T_{s,k+1}]$ ). The supervisory control algorithm is aware of future power harvesting (through solar irradiance prediction) and power consumption in the RTES-EH to perform effective supercapacitor SoC control.

#### A. Motivation

We have the following observations on the RTES-EH:

- 1) At the beginning (i.e., in the morning) and at the end (i.e., in the evening) of the RTES-EH operational period, the solar irradiance level is low; while the solar irradiance becomes abundant in the middle (i.e., at noon) of system operational period in general.
- 2) At the beginning of the RTES-EH operational period, the supercapacitor has no or very little energy—this is due to the effect of self-discharge overnight.
- 3) The supercapacitor terminal voltage varies significantly as a function of the supercapacitor SoC. And the charger and DC-DC converter efficiencies are strongly dependent on the supercapacitor terminal voltage.

Based on the above observations, we have the following motivations for the proposed global control algorithm.

- 1) There exists a desirable amount of supercapacitor energy, such that the task instance drop rate can be minimized if the amount of energy stored in the supercapacitor is close to such a desirable value, due to the converter efficiency variation. The desirable energy value varies according to the solar irradiance change during a day.
- 2) Selectively dropping some task instances at the beginning of the RTES-EH operational period may eventually help increase the total number of completely executed task instances since the energy stored in the supercapacitor may increase (towards the desirable value) along with system operation.
- 3) It is desirable to use up the energy in the supercapacitor by the time  $T_{sunset}$ , since the supercapacitor energy will be eventually dissipated due to self-discharge at night.

#### B. Outer Supervisory Control Loop

The objective of the supervisory control is to maintain the amount of supercapacitor energy (or equivalently, its SoC) around or above a desirable value, through effective task scheduling with DVFS as well as selective task instance dropping. In order to effectively perform supervisory control

at each decision epoch, we first identify two new subproblems and provide corresponding solutions: the *converter-aware task scheduling* (CA-TS) problem (without task instance dropping) and the *supercapacitor energy control* (SEC) problem. Then we provide the supervisory control algorithm based on the solutions to the two subproblems, the above-described motivations, as well as effective solar irradiance prediction. Fig. 6 illustrates the relationship between the control algorithms and the subproblems in this paper in order for better understanding. As can be seen from Fig. 6, the previously defined SC problem and CA-FS problem are fundamental to the solutions to the CA-TS problem and the SEC problem, which are basics steps for the supervisory control loop.

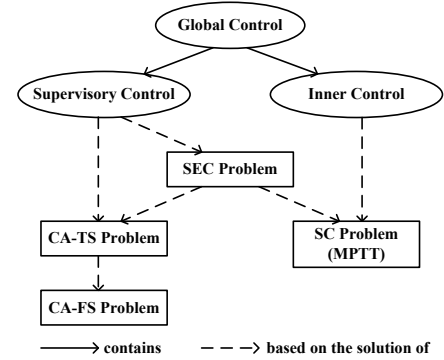


Fig. 6. The relationship between control algorithms and subproblems.

#### 1) Converter-Aware Task Scheduling (CA-TS) Problem

Suppose we are at the  $k$ -th decision epoch  $T_{s,k}$ . The supercapacitor energy and terminal voltage are given by  $E_{cap}(T_{s,k})$  and  $V_{cap}(T_{s,k})$ , respectively. We are given a set of task instances, denoted by  $\mathfrak{I}$ . The absolute release time and absolute deadline of all task instances in  $\mathfrak{I}$  are within the time period  $[T_{s,k}, T_{s,k+1}]$  (the  $k$ -th frame.) We are going to find a schedule and frequency allocation of all the task instances in  $\mathfrak{I}$ , such that the amount of energy extracted from the supercapacitor is minimized. Please note that task instance dropping is not allowed in this problem.

The method in [6] finds the optimal schedule and frequency allocation of a set of task instances on a continuously variable frequency processor, satisfying deadline constraints but without taking into account the converter power loss. On the other hand, the CA-FS problem proposed in Section V.B finds the optimal sensor node frequency for executing a specific task instance, taking into account the converter power loss but without any deadline constraint. Combining the method in [6] and the CA-FS problem, we can generate the optimal schedule and frequency allocation of a set of task instances satisfying deadline constraints and minimizing the energy extracted from the supercapacitor by considering the converter power loss. However, such allocated frequency levels are continuous variables. Then we employ the idea in [28] to use at most two discrete frequency levels for each task instance, and the two frequency levels are immediate neighbors of the continuous frequency level allocated previously.

Details of the proposed solution to the CA-TS problem are given in Algorithm 1. Similar to the solution to the CA-FS problem, we make the assumption in Algorithm 1 that the supercapacitor voltage will not change significantly during the time period  $[T_{s,k}, T_{s,k+1}]$  (the  $k$ -th frame). Based on this assumption, Algorithm 1 will provide the optimal discretely variable frequency allocation and schedule for all task instances considering the DC-DC converter power loss.

---

**Algorithm 1: Solution to the CA-TS Problem.**


---

Generate an optimal continuously variable frequency allocation and schedule for all task instances in  $\mathfrak{I}$ , using the method in [6].

Find the optimal sensor node execution frequencies for task instances of  $\mathcal{T}_i$ , i.e.,  $f_i^{opt}(V_{cap}(T_{s,k}))$  for  $1 \leq i \leq M$ , by optimally solving the CA-FS problem.

**For** each task instance:

**If** the allocated frequency is less than  $f_i^{opt}(V_{cap}(T_{s,k}))$ :

Allocate the frequency  $f_i^{opt}(V_{cap}(T_{s,k}))$  to that task instance.

Use the algorithm proposed in [28] to generate the optimal discretely variable frequency allocation and schedule for all task instances in  $\mathfrak{I}$ .

**Return** the schedule and frequency allocation.

---

### 2) Supercapacitor Energy Control (SEC) Problem

Suppose we are at the  $k$ -th decision epoch  $T_{s,k}$ . The SEC problem aims to find the optimal amount of supercapacitor energy in the  $k$ -th frame, denoted by  $E_{cap,k}^{tar}$ , such that the RTES-EH system availability will be maximized (i.e., the task instance drop rate will be minimized) when the amount of supercapacitor energy is near such a desirable value. In the following we discuss about the equivalent problem of finding the optimal supercapacitor terminal voltage  $V_{cap,k}^{tar}$ .

For each possible supercapacitor terminal voltage value  $V_{cap}$ , we calculate the *estimated system availability* as follows. For simplicity in estimation and without significant loss of accuracy, we assume that the supercapacitor terminal voltage will not change significantly (i.e.,  $V_{cap}(t) \approx V_{cap}$ ). The estimated input energy of the supercapacitor from the  $k$ -th frame to the  $K$ -th frame as a function of  $V_{cap}$ , denoted by  $\hat{E}_{in,k,total}(V_{cap})$ , is calculated using

$$\hat{E}_{in,k,total}(V_{cap}) = V_{cap} \cdot \int_{T_{s,k}}^{T_{sunset}} \max_{(V_{pv}(t), I_{pv}(t)); V_{cap}(t)=V_{cap}} I_{cap,in}(t) dt, \quad (20)$$

where the (estimated) supercapacitor input current  $I_{cap,in}(t)$  is maximized by finding the optimal PV panel operating point  $(V_{pv}(t), I_{pv}(t))$  (i.e., optimally solving the SC problem) based on the predicted solar irradiance profile. Note that this is the software/model-based solution to the SC problem as described in Section V.A.

Next we calculate the estimated output energy of the supercapacitor. We derive the schedule and frequency allocation for task instances in the  $k$ -th frame, represented by  $f_{s_i}(t)$  for  $1 \leq i \leq M$  and  $t \in [T_{s,k}, T_{s,k+1}]$ , by solving the CA-TS problem, in which we assume that the supercapacitor terminal voltage is  $V_{cap}$ . We calculate the (estimated) supercapacitor discharging current  $I_{cap,out}(t)$  based on  $f_s(t) = \sum_{1 \leq i \leq M} f_{s_i}(t)$  and  $V_{cap}$ , in the way described in Section IV. The estimated output energy of the supercapacitor during the  $k$ -th frame as a function of  $V_{cap}$ , denoted by  $\hat{E}_{out,k}(V_{cap})$ , is calculated using

$$\hat{E}_{out,k}(V_{cap}) = V_{cap} \cdot \int_{T_{s,k}}^{T_{s,k+1}} I_{cap,out}(t) dt. \quad (21)$$

Since the supercapacitor voltage is assumed to be a constant value  $V_{cap}$ , the estimated output energy of the supercapacitor over each  $\hat{k}$ -th frame ( $k < \hat{k} \leq K$ ) is also equal to  $\hat{E}_{out,k}(V_{cap})$ .

The estimated self-discharge energy loss in the supercapacitor from the  $k$ -th frame to the  $K$ -th frame as a function of  $V_{cap}$ , denoted by  $\hat{E}_{sd,k,total}(V_{cap})$ , is calculated using:

$$\begin{aligned} \hat{E}_{sd,k,total}(V_{cap}) &= V_{cap} \cdot I_{cap,sd}(V_{cap}) \cdot (T_{sunset} - T_{s,k}) \\ &= (K - k + 1) \cdot C_{cap} \cdot \frac{(V_{cap})^2}{r} \cdot T_{LCM}, \end{aligned} \quad (22)$$

where  $I_{cap,sd}(V_{cap})$  is the supercapacitor self-discharge current as a function of  $V_{cap}$ . The above equation is derived from (8).

We define the ratio of  $\hat{E}_{in,k,total}(V_{cap}) - \hat{E}_{sd,k,total}(V_{cap})$  to  $\hat{E}_{out,k}(V_{cap})$  as the *estimated system availability*. The estimated system availability represents the estimated number of frames that can be executed in the sensor node during the time period  $[T_{s,k}, T_{sunset}]$ . The optimal (target) supercapacitor terminal voltage  $V_{cap,k}^{tar}$  is the optimal  $V_{cap}$  value that maximizes the estimated system availability. Therefore,  $V_{cap,k}^{tar}$  is calculated by

$$V_{cap,k}^{tar} = \operatorname{argmax}_{V_{cap}} \frac{\hat{E}_{in,k,total}(V_{cap}) - \hat{E}_{sd,k,total}(V_{cap})}{\hat{E}_{out,k}(V_{cap})}. \quad (23)$$

### 3) Supervisory Control Algorithm

The objective of the supervisory control algorithm is to maintain the amount of supercapacitor energy (or equivalently, its SoC) around or above a desirable value, through effective task scheduling with DVFS as well as selective task instance dropping. Consider the supervisory control algorithm performed at the decision epoch  $T_{s,k}$ . The supercapacitor energy and terminal voltage are given by  $E_{cap}(T_{s,k})$  and  $V_{cap}(T_{s,k})$ , respectively. The optimal (target) supercapacitor energy is given by  $E_{cap,k}^{tar}$ , satisfying  $E_{cap,k}^{tar} = \frac{1}{2} C_{cap} (V_{cap,k}^{tar})^2$ . We use  $e_{cap,k} = E_{cap}(T_{s,k}) - E_{cap,k}^{tar}$  to denote the difference



between the amount of supercapacitor energy and the target value. The supervisory control algorithm goes as follows:

**Case I** ( $e_{cap,k} \geq 0$ ): In this case the amount of energy stored in the supercapacitor is abundant (higher than the target value.) We schedule all the task instances in the  $k$ -th frame using Algorithm 1, without task instance dropping.

**Case II** ( $e_{cap,k} < 0$ ): In this case the objective of the supervisory control algorithm is to make the supercapacitor energy at the next decision epoch,  $E_{cap}(T_{s,k+1})$ , equal to or higher than the value  $E_{cap}(T_{s,k}) + \delta \cdot |e_{cap,k}|$ , in which  $\delta$  is a predefined feedback control parameter. We may have to drop some task instances to achieve this goal. The basic idea is to keep dropping the most energy consuming task instance and performing task rescheduling using Algorithm 1, until the estimated amount of energy stored in the supercapacitor at time  $T_{s,k+1}$  satisfies the requirement. Detailed procedure is shown in Algorithm 2.

However, there is no need for keeping the supercapacitor energy around or above the target value near the end of the RTES-EH operational period (i.e., in the evening.) We can schedule all the task instances without dropping in this case. We use the following estimation-based procedure to decide at a decision epoch  $T_{s,k}$  whether performing supercapacitor energy maintenance is necessary. We first calculate the estimated supercapacitor input energy  $\hat{E}_{in,k,total}(V_{cap}(T_{s,k}))$  and self-discharge energy loss  $\hat{E}_{sd,k,total}(V_{cap}(T_{s,k}))$  using the method described in Section VII.B.2). Next we calculate the estimated supercapacitor output energy  $\hat{E}_{out,k,total}(V_{cap}(T_{s,k}))$  as

$$\hat{E}_{out,k,total}(V_{cap}(T_{s,k})) = (K - k + 1)\hat{E}_{out,k}(V_{cap}(T_{s,k})), \quad (24)$$

where  $\hat{E}_{out,k}(V_{cap}(T_{s,k}))$  is calculated in the way described in (21). If  $\hat{E}_{in,k,total}(V_{cap}(T_{s,k})) + E_{cap}(T_{s,k}) \geq \hat{E}_{out,k,total}(V_{cap}(T_{s,k})) + \hat{E}_{sd,k,total}(V_{cap}(T_{s,k}))$ , we conclude that the supercapacitor energy plus the future harvested energy is enough for scheduling all the task instances until  $T_{sunset}$ , and hence the supervisory control algorithm will schedule all the task instances in the  $k$ -th frame without task instance dropping. Otherwise, we perform supercapacitor energy maintenance based on selective task instance dropping. Details of the proposed supervisory control algorithm are given in Algorithm 2. We again make the assumption that the supercapacitor terminal voltage will not change significantly during the  $k$ -th frame.

---

**Algorithm 2: The Supervisory Control Algorithm.**


---

Predict the solar irradiance levels of the rest of the frames in the day, i.e., if  $k=1$ , calculate  $Predict_k^d$  for  $k \leq \hat{k} \leq K$ ; otherwise, calculate  $Refine_k^d$  for  $k \leq \hat{k} \leq K$ .

Calculate the  $\hat{E}_{in,k,total}(V_{cap}(T_{s,k}))$ ,  $\hat{E}_{out,k,total}(V_{cap}(T_{s,k}))$ ,

---

and  $\hat{E}_{sd,k,total}(V_{cap}(T_{s,k}))$ .

Initialize the set  $\mathfrak{Z}$  to include all task instances in the  $k$ -th frame.

**If**  $\hat{E}_{in,k,total}(V_{cap}(T_{s,k})) + E_{cap}(T_{s,k}) \geq \hat{E}_{out,k,total}(V_{cap}(T_{s,k})) + \hat{E}_{sd,k,total}(V_{cap}(T_{s,k}))$ :

Use Algorithm 1 to generate a schedule for all task instances in  $\mathfrak{Z}$ .

**Else:**

Calculate  $E_{cap,k}^{tar}$  by solving the SEC problem.

Calculate  $e_{cap,k} = E_{cap}(T_{s,k}) - E_{cap,k}^{tar}$ .

**If**  $e_{cap,k} \geq 0$ :

Use Algorithm 1 to generate a schedule of all task instances in  $\mathfrak{Z}$ .

**Else:**

Calculate the estimated supercapacitor input energy during the  $k$ -th frame, given by  $\hat{E}_{in,k}(V_{cap}(T_{s,k})) = V_{cap}(T_{s,k}) \cdot$

$$\int_{T_{s,k}}^{T_{s,k+1}} \max(V_{pv}(t), I_{pv}(t); V_{cap}(t) = V_{cap}(T_{s,k})) I_{cap,in}(t) dt.$$

Calculate the estimated supercapacitor self-discharge energy loss during the  $k$ -th frame, given by

$$\hat{E}_{sd,k}(V_{cap}(T_{s,k})) = C_{cap} \frac{(V_{cap}(T_{s,k}))^2}{\Gamma} T_{LCM}.$$

Use Algorithm 1 to generate a schedule of all task instances in  $\mathfrak{Z}$ .

Calculate the estimated supercapacitor output energy  $\hat{E}_{out,k}(V_{cap}(T_{s,k}))$  during the  $k$ -th frame based on the schedule.

**While**  $E_{cap}(T_{s,k}) + \hat{E}_{in,k}(V_{cap}(T_{s,k})) - \hat{E}_{out,k}(V_{cap}(T_{s,k})) - \hat{E}_{sd,k}(V_{cap}(T_{s,k})) < E_{cap}(T_{s,k}) + \delta \cdot |e_{cap,k}|$ :

Drop the most energy consuming task instance from  $\mathfrak{Z}$ .

Use Algorithm 1 to generate a schedule for the new set  $\mathfrak{Z}$ .

Calculate  $\hat{E}_{out,k}(V_{cap}(T_{s,k}))$  based on the new schedule.

**Return** the schedule and frequency allocation.

---

### C. Inner Control Loop

The inner control loop determines the optimal I-V operating point of the PV panel (and hence the input current of the supercapacitor). The inner control loop is performed every five milliseconds in this paper. At time  $t$ , the supercapacitor energy is given by  $E_{cap}(t)$ . The inner control loop determines the optimal PV panel operating point  $(V_{pv}(t), I_{pv}(t))$  by optimally solving the SC problem based on the actual solar irradiance  $G(t)$ . Please note that this is the hardware-based solution to the SC problem as described in Section V.A. Besides, the sensor node execution frequency  $fs(t)$  is given by the task schedule and frequency allocation generated by the

supervisory control algorithm. The inner control loop also controls the sensor node supply voltage  $V_{proc}(t)$  using the DC-DC converter, so that the embedded sensor node properly runs at frequency  $fs(t)$ .

### VIII. EXPERIMENTAL RESULTS

First, we need to test the accuracy of our solar irradiance prediction algorithm. We use the solar irradiance profiles measured at Duffield, VA, for the year of 2007. Remember that the initial prediction for the sunny day solar irradiance is based on the actual solar irradiance in the previous day, and therefore, we use the solar irradiance profiles for the first 91 days in the year as the training data and we predict the solar irradiance for the rest of days in the year.

Fig. 7 shows the actual and predicted solar irradiance profiles of day 170, 230, 290, and 350 at Duffield, VA in the year of 2007. Please note that the solar irradiance levels are normalized by the solar irradiance value  $G_{STC}$  at standard test condition. Fig. 7 contains the actual solar irradiance profiles, the initial prediction result, and the refined prediction result. Remember that the initial prediction is performed at the beginning of each day (i.e., 6:00am in this work) and the intra-day refinement is performed at the start time of each  $k$ -th (for  $1 < k \leq K$ ) frame in a day. In Fig. 7, the refined prediction result for the  $k$ -th frame in a day is obtained (and refined for the last time) at the start time of the  $k$ -th frame. We can observe from Fig. 7 that (i) in a sunny day (e.g., day 290) the initial prediction is accurate enough and the intra-day refinement cannot improve accuracy further and (ii) in a “cloudy” day the intra-day refinement improves prediction accuracy significantly. On average, the prediction error of initial prediction is 19.4% and the prediction error of refined prediction is 8.1%.

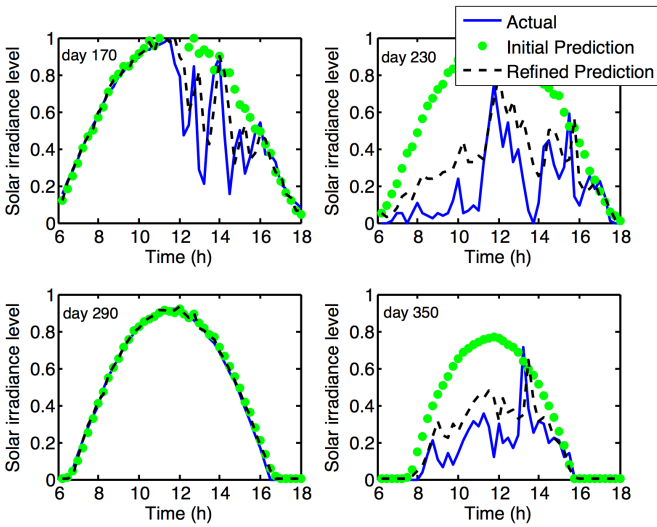


Fig. 7. The actual and predicted solar irradiance profiles of four different days (day 170, 230, 290, and 350) at Duffield, VA in the year of 2007.

In the next, we compare our proposed global control algorithm with a baseline control algorithm on the RTES-EH

in terms of task instance drop rate. The PV panel used in the RTES-EH has a maximum output current of 0.305 A, a maximum output voltage of 27.8 V, and an MPP output power of 6.2 W under the standard test condition. The I-V and P-V characteristics of the PV panel are shown in Fig. 5. We use the Linear Technology LTM4607 converter as the charger and voltage converter model in the RTES-EH. A 500 F supercapacitor is used as the energy storage device. The embedded sensor node in the RTES-EH has six discrete operating frequencies: 500 MHz, 600 MHz, 700 MHz, 800 MHz, 900 MHz, and 1000 MHz. Correspondingly, the sensor node has six discrete supply voltage levels: 1.0 V, 1.2 V, 1.4 V, 1.6 V, 1.8 V, and 2.0 V, and six power levels: 0.62 W, 0.89 W, 1.21 W, 1.58 W, 2.00 W, and 2.47 W. The task set executed in the RTES-EH consists of five tasks i.e.,  $T_1, T_2, \dots, T_5$ , the periods  $D_i$  ( $1 \leq i \leq 5$ ) of which are 50 s, 60 s, 100 s, 150 s, and 300 s, respectively. The frame length  $T_{LCM}$ , which is the *hyper-period* of all the tasks, is therefore 300 s in the RTES-EH. The task instance execution times i.e.,  $W_i/freq_{max}$  ( $1 \leq i \leq 5$ ), which is the execution time of an task instance of  $T_i$  when the sensor node runs at its maximum operating frequency  $freq_{max}$ , are 10 s, 10 s, 15 s, 15 s, and 30 s, respectively. The above task setup is based on habitat monitoring sensor node [26] and wireless camera sensor node [27]. The baseline control algorithm is based on the same RTES-EH system architecture. The baseline algorithm adopts [28] to find a discretely variable frequency allocation and schedule of all task instances in the sensor node, and incorporates a simple procedure to protect the supercapacitor from energy depletion. When the sensor node is about to execute a new task instance, the baseline controller checks whether the current supercapacitor terminal voltage is less than a predefined threshold value. If so, that task instance will be dropped.

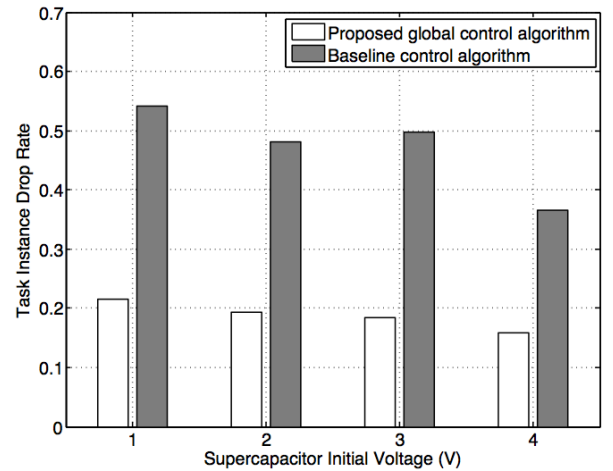


Fig. 8. Task instance drop rate from the proposed global control algorithm and baseline control algorithm based on solar irradiance profile of day 170.

Fig. 8 and Fig. 9 demonstrate the task instance drop rate from the proposed global control algorithm and the baseline control algorithm when the solar irradiance profiles of day 170 and day 290 are used, respectively. The task instance drop rate

for different supercapacitor initial voltage  $V_{cap}(T_{sunrise})$  levels (i.e., from 1 V to 4 V) are plotted in Fig. 8 and Fig. 9. Please note that the proposed global control algorithm is based on the solar irradiance prediction results, whereas the baseline control algorithm is based on instantaneous solar irradiance level. We can observe that the proposed global control algorithm consistently outperforms the baseline control algorithm. The proposed global control algorithm achieves a maximum of 63% reduction in task instance drop rate compared with the baseline algorithm.

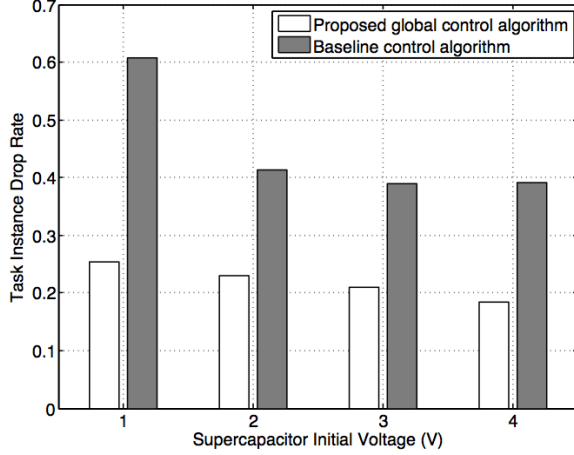


Fig. 9. Task instance drop rate from the proposed global control algorithm and baseline control algorithm based on solar irradiance profile of day 290.

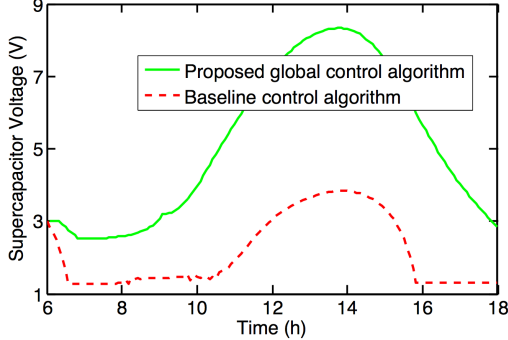


Fig. 10. Supercapacitor terminal voltage change from  $T_{sunrise}$  to  $T_{sunset}$  (i.e., a system operational period).

Furthermore, we examine the supercapacitor terminal voltage  $V_{cap}(t)$  change and number of dropped task instances during a system operational period (from  $T_{sunrise}$  to  $T_{sunset}$ ) shown in Fig. 10 and Fig. 11, respectively. Combining the information in Fig. 10 and Fig. 11, we can find that at the beginning of the system operational period the baseline control algorithm tends to execute all the task instances until  $V_{cap}(t)$  drops to a threshold value, whereas the proposed global control algorithm is more conservative by dropping some task instances even though the supercapacitor has enough initial energy. After some time, the supercapacitor in the global control algorithm can accumulate higher energy than the supercapacitor in the baseline control algorithm when the solar irradiance is abundant (at noon). Therefore, the global control algorithm can maintain a lower task instance

drop rate in the late afternoon (when the solar irradiance is not abundant).

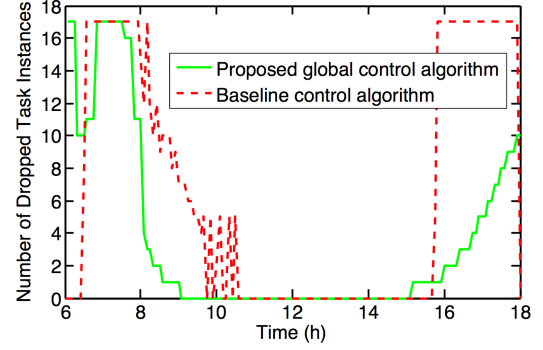


Fig. 11. Number of dropped task instances per frame length  $T_{LCM}$  from  $T_{sunrise}$  to  $T_{sunset}$  (i.e., a system operational period).

In addition, we demonstrate the difference between the task instance drop rates from the proposed global control algorithm when using the predicted and actual solar irradiance profile in Fig. 12. The solar irradiance profile of day 230 in Fig. 7 is used for the simulation. There are two observations from Fig. 12. First, the general task instance drop rates are higher compared with the results in Fig. 8 and Fig. 9. This is due to the relatively low solar irradiance in day 230. Second, the task instance drop rate from the proposed global control algorithm using predicted solar irradiance profile is slightly higher than that using actual solar irradiance profile. It demonstrates that our proposed global control algorithm is robust under solar irradiance prediction error.

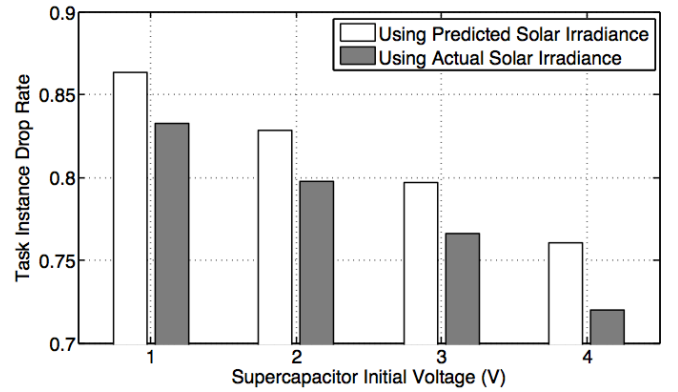


Fig. 12. Task instance drop rate from the proposed global control algorithm using predicted and actual solar irradiance profile of day 230.

## IX. CONCLUSION

In this paper, we investigate the question of how one can achieve the prolonged lifespan of a real-time embedded system with energy harvesting capability by applying a global control strategy. The global controller performs optimal operating point tracking for the PV panel, SoC management for the supercapacitor, and energy-harvesting-aware real-time task scheduling with DVFS for the sensor node, based on an accurate solar irradiance prediction method. The controller, which accounts for dynamic I-V characteristics of the PV

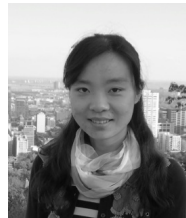
panel, terminal voltage variation and self-discharge of the supercapacitor, and power losses in power converters, employs a cascaded feedback control structure with an inner control loop determining the I-V operating point of the PV panel and an outer supervisory control loop performing real-time task scheduling and setting the voltage and frequency levels in the sensor node.

#### ACKNOWLEDGMENTS

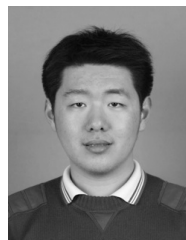
This work is support in part by a grant from the Software and Hardware Foundations of the National Science Foundation, and the Center for Integrated Smart Sensors funded by Science, ICT & Future Planning as Global Frontier Project (CISS-N01140838).

#### REFERENCES

- [1] X. Lin, Y. Wang, S. Yue, N. Chang, and M. Pedram, "A framework of concurrent task scheduling and dynamic voltage and frequency scaling in real-time embedded systems with energy harvesting," in *ISLPED*, Beijing, China, 2013, pp. 70-75.
- [2] Y.H. Lu, L. Benini, and G. De Micheli, "Low-power task scheduling for multiple devices," in *CODES*, San Diego, CA, 2000, pp. 39-43.
- [3] Q. Qiu, S. Liu, and Q. Wu, "Task merging for dynamic power management of cyclic applications in real-time multiprocessor systems," in *ICCD*, San Jose, CA, 2006, pp. 397-404.
- [4] R. Mishra, N. Rastogi, et al., "Energy aware scheduling for distributed real-time systems," in *IPDPS*, Nice, France, 2003.
- [5] Y. Wang, Q. Xie, A. Ammari, and M. Pedram, "Deriving a near-optimal power management policy using model-free reinforcement learning and Bayesian classification," in *DAC*, San Diego, CA, 2011, pp. 41-46.
- [6] F. Yao, A. Demers, and S. Shenker, "A scheduling model for reduced CPU energy," in *SFCS*, Milwaukee, WI, 1995, pp. 374-382.
- [7] T. Ishihara, and H. Yasuura, "Voltage scheduling problem for dynamically variable voltage processors," in *ISLPED*, Monterey, CA, 1998, pp. 197-202.
- [8] G. Quan, and X. S. Hu, "Minimum energy fixed-priority scheduling for variable voltage processors," *IEEE Trans. CAD*, vol. 22, no. 8, pp. 1062-1071, Aug. 2003.
- [9] J. Luo, and N.K. Jha, "Static and dynamic variable voltage scheduling algorithms for real-time heterogeneous distributed embedded systems," in *ASP-DAC*, Bangalore, India, 2002, pp. 719.
- [10] V. Raghunathan, A. Kansal, J. Hsu, J. Friedman, and M. Srivastava, "Design considerations for solar energy harvesting wireless embedded systems," in *IPSN*, Los Angeles, CA, 2005, pp. 457-462.
- [11] X. Jiang, J. Polastre, and D. Culler, "Perpetual environmentally powered sensor networks," in *IPSN*, Los Angeles, CA, 2005, pp. 463-468.
- [12] F. Simjee, and P.H. Chou, "Everlast; long-life, supercapacitor-operated wireless sensor node," in *ISLPED*, Tegernsee, Germany, 2006, pp. 197-202.
- [13] A. Kansal, J. Hsu, et al., "Harvesting aware power management for sensor networks," in *DAC*, San Francisco, CA, 2006, pp. 651-656.
- [14] C. Moser, D. Brunelli, et al., "Lazy scheduling for energy harvesting sensor nodes," in *DIPES*, Braga, Portugal, 2006, pp. 125-134.
- [15] S. Liu, Q. Qiu, and Q. Wu, "Energy aware dynamic voltage and frequency selection for real-time systems with energy harvesting," in *DATE*, Munich, Germany, 2008, pp. 236-241.
- [16] S. Liu, Q. Wu, and Q. Qiu, "An adaptive scheduling and voltage/frequency selection algorithm for real-time energy harvesting systems," in *DAC*, San Francisco, CA, 2009, pp. 782-787.
- [17] M. Pedram, N. Chang, Y. Kim, and Y. Wang, "Hybrid electrical energy storage systems," in *ISLPED*, Austin, TX, 2010, pp. 363-368.
- [18] Y. Kim, N. Chang, Y. Wang, and M. Pedram, "Maximum power transfer tracking for a photovoltaic-supercapacitor energy system," in *ISLPED*, Austin, TX, 2010, pp. 307-312.
- [19] C. Lu, V. Raghunathan, and K. Roy, "Maximum power point considerations in micro-scale solar energy harvesting systems," in *ISCAS*, Paris, France, 2010, pp. 273-276.
- [20] T. Eseram, J.W. Kimball, et al., "Dynamic maximum power point tracking of photovoltaic arrays using ripple correlation control," *IEEE Trans. Power Electronics*, vol. 21, no. 5, pp. 1282-1291, Sept. 2006.
- [21] Y. Choi, N. Chang, and T. Kim, "DC-DC converter-aware power management for low-power embedded systems," *IEEE Trans. CAD*, vol. 26, no. 8, pp. 1367-1381, Aug. 2007.
- [22] W. Lee, Y. Kim, Y. Wang, N. Chang, M. Pedram, and S. Han, "Versatile high-fidelity photovoltaic module emulation system," in *ISLPED*, Fukuoka, Japan, 2011, pp. 91-96.
- [23] Y. Wang, Y. Kim, Q. Xie, N. Chang, and M. Pedram, "Charge migration efficiency optimization in hybrid electrical energy storage (HEES) systems," in *ISLPED*, Fukuoka, Japan, 2011, pp. 103-108.
- [24] Y. Wang, S. Yue, M. Pedram, L. Kerofsky, and S. Deshpande, "A hierarchical control algorithm for managing electrical energy storage systems in homes equipped with PV power generation," in *Green Technologies Conference*, Tulsa, OK, 2012, pp. 1-6.
- [25] C. M. Bishop, *Pattern Recognition and Machine Learning*, Springer, August 2006.
- [26] A. Mainwaring, J. Polastre, R. Szewczyk, D. Culler, and J. Anderson, "Wireless sensor networks for habitat monitoring," in *WSNA*, Atlanta, Georgia, 2002, pp. 88-97.
- [27] Y. Jin, S. Vural, A. Gluhak, and K. Moessner, "Dynamic task allocation in multi-hop multimedia wireless sensor networks with low mobility," *Sensors*, vol. 13, no. 10, pp. 13998-14028, 2013.
- [28] W. Kwon, and T. Kim, "Optimal voltage allocation techniques for dynamically variable voltage processors," in *DAC*, Anaheim, CA, 2003, pp. 125-130.



systems, (ii) near-threshold computing for low-power embedded systems, and (iii) machine learning and computing in cyber-physical systems. She has published about 50 papers in these areas.



Department of Electrical Engineering and Computer Science at Syracuse University. His research interests include neuromorphic computing, next generation energy generation/storage and applications, low-power circuits and systems design, etc. He has published more than 100 papers in these areas. He received the best paper awards at 2014 IEEE International Symposium on VLSI (ISVLSI) and 2014 IEEE/ACM International Symposium on Low Power Electronics Design (ISLPED).

**Xue Lin** (S'12) received her B.S. degree from Tsinghua University, Beijing, China, in 2009. She is now a Ph.D. candidate in the Department of Electrical Engineering at University of Southern California. Her advisor is Prof. Massoud Pedram. She has been working on (i) high-performance computing and mobile cloud computing

**Yanzhi Wang** (S'12) received his B.S. degree with distinction in electronic engineering from Tsinghua University, Beijing, China, in 2009, and Ph.D. degree in electrical engineering at University of Southern California, in 2014, under the supervision of Prof. Massoud Pedram. He is currently an assistant professor in the





**Naehyuck Chang** (F'12) received the B.S., M.S. and Ph.D. degrees from the Department of Control and Instrumentation, Seoul National University, Seoul, Korea, in 1989, 1992, and 1996, respectively. Dr. Chang is a Full Professor at the Department of Electrical Engineering, Korea Advanced Institute of Science and Technology (KAIST) from 2014. Before he joined KAIST, he was with the Department of Computer Science and Engineering, Seoul National University from 1997 to 2014. Dr. Chang also served as a Vice Dean of College of Engineering, Seoul National University from 2011 to 2013. His current research interests include low-power embedded systems and Design Automation of Things such as systematic design and optimization of energy storage systems and electric vehicles.

Dr. Chang is the Editor-in-Chief of the ACM Transactions on Design Automation of Electronics Systems, and an Associate Editor of IEEE Transactions on Very Large Scale Integration Systems. He also served for IEEE Transactions on Computer-Aided Design of Integrated Circuits and Systems, IEEE Embedded Systems Letters, ACM Transactions on Embedded Computing Systems, and so on, as an Associate Editor. Dr. Chang is (was) the General Co-Chair of VLSI-SoC, ICCD 2014 and 2015, ISLPED 2011, etc. Dr. Chang is (was) Technical Program (Co-) Chair of DAC 2016, ASP-DAC 2015, ICCD 2014, CODES+ISSS 2012, ISLPED 2009, etc. Dr. Chang is an ACM Fellow.

Dr. Chang is a recipient of several ISLPED low-power design contest awards, 2012 SAE Vincent Bendix Automotive Electronics Engineering Award, 2014 ISLPED Best Paper Award, 2009 IEEE SSCS Seoul Chapter Award, etc. Dr. Chang was LG Yonam Foundation Research Professor in 2005.

committee of a number of premiere conferences in his field and was the founding Technical Program Co-chair of the 1996 International Symposium on Low Power Electronics and Design and the Technical Program Chair of the 2002 International Symposium on Physical Design.



**Massoud Pedram** (F'01), who is the Stephen and Etta Varra Professor in the Ming Hsieh department of Electrical Engineering at University of Southern California, received a Ph.D. in Electrical Engineering and Computer Sciences from the University of California, Berkeley in 1991. He holds 10 U.S. patents and has published four books, 13 book chapters, and more than 140 archival and 380 conference papers. His research ranges from low power electronics, energy-efficient processing, and cloud computing to photovoltaic cell power generation, energy storage, and power conversion, and from RT-level optimization of VLSI circuits to synthesis and physical design of quantum circuits. For this research, he and his students have received seven conference and two IEEE Transactions Best Paper Awards. Dr. Pedram is a receipt of the 1996 Presidential Early Career Award for Scientists and Engineers, a Fellow of the IEEE, an ACM Distinguished Scientist, and currently serves as the Editor-in-Chiefs of the ACM Transactions on Design Automation of Electronic Systems and the IEEE Journal on Emerging and Selected Topics in Circuits and Systems. He has also served on the technical program